Prediction of the laminar-to-turbulent transition position on a helicopter rotor in forward flight

Francois Richez, Rohit Jain

PREDICTION OF THE LAMINAR-TO-TURBULENT TRANSITION POSITION ON A HELICOPTER ROTOR IN FORWARD FLIGHT

François Richez
ONERA/The French Aerospace Lab
Meudon, France

Rohit Jain
U.S. Army Combat Capabilities Development Command
Aviation & Missile Center
Moffett Field, CA, USA

ABSTRACT

This paper proposes to evaluate the capabilities of different turbulence transition models with CREATE™-AV Helios and elsA CFD codes to reproduce the boundary layer transition evolution on a helicopter rotor blade in forward flight. Transition models based on transport equations such as Amplification Factor Transport model and Langtry-Menter model provide good agreements with the experimental measurements, while models based on semi-empirical boundary layer criteria show more discrepancies. The sensitivity of the prediction with respect to the numerical setup is analyzed. It shows that the grid resolution and the blade deformation have a noticeable effect on the transition position, while the fuselage has a minor influence. The strategy used to compute the transition position has to be set up carefully as it can significantly impact the results. With the same Langtry-Menter model, Helios and elsA shows similar predictions, but Helios provides a better agreement with experiments that can be partially related to the blade deformation.

NOTATION

Symbols

b	Number of blade
c	Blade chord, m
C_T/σ	Thrust coefficient, $T/[\rho S\sigma(R\Omega)^2]$
k	Turbulent kinetic energy, m^2/s^2
$M_{R\Omega}$	Hover tip Mach number, $R\Omega/V_s$
Q	Q-criterion
R	Rotor radius, m
S	Rotor area, πR^2, m^2
T	Rotor thrust, N
V_s	Freestream sound speed, m/s
x_{tr}	Chordwise transition position, m
$\beta_0, \beta_{1c}, \beta_{1s}$	Flap angles, deg
$\delta_0, \delta_{1c}, \delta_{1s}$	Lead-lag angles, deg
$\theta_0, \theta_{1c}, \theta_{1s}$	Pitch angles, deg
μ_t/μ	Eddy viscosity ratio
ω	dissipation rate of k, s^{-1}
Ω	Rotor speed of rotation, rad/s

Acronyms

CFD	Computational Fluid Dynamics
DIT	Differential Infrared Thermography
RANS	Reynolds Averaged Navier-Stokes
DDES	Delayed Detached Eddy Simulation
TC	Transition Criteria (Ref. 2)
LM	Langtry-Menter (Ref. 3)
LM-G	Langtry-Menter model with Galilean invariance correction
LM-G-CF	LM-G including Crossflow Correlation
SA	Spalart-Allmaras model (Ref. 19)
SST	Shear-Stress Transport k-ω model (Ref. 20)

Presented at the 50th European Rotorcraft Forum, Marseille, France, September 10-12, 2024.

1. INTRODUCTION

Large regions of laminar boundary layer flow could appear on helicopter rotor blades. As the skin friction force is lower in a laminar boundary layer compared to its turbulent counterpart, these laminar regions lead to a significant reduction of the blade profile drag power. Most of CFD (Computational Fluid Dynamics) simulations of helicopter

rotor flows are based on a RANS (Reynolds-Averaged Navier-Stokes) or DDES (Delayed Detached Eddy Simulation) approaches that assume the boundary layer flows as fully turbulent from the stagnation point up to the trailing edge of the blades. Thus, these kinds of numerical simulations tend to overestimate the rotor power. In order to improve the prediction of the rotor performance, it is required to take into account the laminar-to-turbulent transition process in the RANS or DDES modeling. Several methods for transition modeling exist in the literature. Some are based on semi-empirical criteria that are deduced from wall quantities to deactivate the turbulence model in the flow regions expected as laminar. This kind of approach, defined as Transition Criteria (TC) thereafter, is known to be accurate for a large variety of flows (Refs. 1 and 2). However, the TC method is not straightforward as it is a complex process to first compute the laminar and turbulent regions at the walls and then to propagate this information into the three-dimensional fluid domain. Another kind of transition models is based on the addition of transport equations of new quantities to the turbulence model. These new quantities directly impose the laminar or turbulent state of the flow in every grid cell of the fluid domain, which eases the process. One of the most famous transport-equation-based transition models was proposed by Langtry and Menter in Ref. 3 and is referred-to as LM thereafter.

First attempts to model the transition to turbulence in CFD simulations of rotor in hover and forward flights showed that TC model improved the prediction of rotor power while LM seemed to provide mixed results (Ref. 4). However, the experimental data were not accurate enough to evaluate the models in details. Experimental measurements of transition on a small-scale rotor in hover were proposed in Ref. 5 and used as reference by ONERA and DLR in Ref 6 in order to assess TC and LM approaches with elsA and TAU CFD codes. The results also showed good trends of TC method while LM model provided poor correlations with experiments. Later, Jain evaluated LM model with Helios code for the "PSP" rotor in hover (Ref. 7) and showed very good correlations with the experimental measurements of the transition locations (Ref. 8). Based on the experimental data of Weiss et al. (Ref. 9), Jain (Ref. 10) and Carnes *et al.* (Ref. 11) also performed numerical simulations of unsteady cases of the small-scale "RTG" rotor in axial flight with cyclic pitch variations. LM model provided very good prediction of the motion of the transition position as a function of the pitch variation. Finally, all these numerical investigations conducted with different CFD solvers and for different test cases seem to lead to contradictory conclusions concerning LM model. This assessment motivated Richez and Jain to perform a validation analysis of the model with both Helios and elsA codes for the unsteady rotor tested in the DLR (German Aerospace Center) Rotor Test Facility in Göttingen (RTG) (Ref. 12) with pitching blades in axial flow. The authors showed that LM model seemed very sensitive to the numerical parameters and proposed some guidelines required to predict accurately the transition motion on the rotor blades under unsteady conditions. We can additionally expect that the contradictory results observed in the investigations previously mentioned is probably due to differences in the numerical parameters and grid resolution. On the other hand, TC method was less sensitive to the numerical methods but failed to predict the hysteretic behavior of the transition motion observed experimentally during the pitch cycle of the RTG rotor.

In the continuity of this work, we propose in this paper to extend this validation analysis with both Helios and elsA codes to the case of the PSP rotor in forward flight that was experimentally investigated in Ref. 13. The objectives are to assess TC method and LM transition model, evaluate the sensitivity of the solution with respect to numerical parameters and provide some guidelines for transition modeling applied to helicopter rotor flow. This work is a product of a research collaboration on transition modeling under the U.S.-France Project Agreement on Rotary Wing Aeromechanics and Human Factors Integration Research.

2. TEST CASE

The test case is a three-bladed articulated "PSP" rotor mounted on a ROBIN-Mod 7 fuselage (Figure 1). The PSP blade has a radius of $R = 1.7$ m, a linear twist of -14°/R and a chord length of $c = 0.138$ m that reduces to $c_{tip} = 0.083$ m at tip (Table 1). The blade sections are composed of three airfoils from the RC family (Figure 2). The experiment was conducted in the NASA Langley 14- by 22-Foot Subsonic Tunnel. The flight condition corresponds to an advance ratio of $\mu = 0.3$, with a hover Mach tip number of $M_{R\Omega} = 0.555$. The rotor is trimmed to a rotor thrust coefficient $C_T/\sigma = 0.1$ with zero flapping. The evolution of the transition position on the upper side of the blade as a function of the azimuthal angle is measured by Differential Infrared Thermography (DIT). More details of this experimental campaign can be found in Ref. 13.

3. NUMERICAL METHODS

3.1. Helios setup

For numerical simulations, U.S. Army DEVCOM AvMC used the CREATE™-AV Helios software (Ref. 14) which involves NASA OVERFLOW solver (Ref. 15) for the blade body-fitted grids, SAMCART solver for the off-body

Cartesian grids and FUN3D (Ref. 16) for the ROBIN-Mod 7 fuselage near-body grids. The Helios simulation is loosely coupled with the Helicopter comprehensive analysis code RCAS (Ref. 17) in order to reach the desired flight condition ($C_T/\sigma = 0.1$ and zero flapping).

For the blade near-body flow, OVERFLOW solver uses a fifth-order accurate central scheme for the convective fluxes and a second order central scheme for the viscous fluxes. For time integration, a second-order diagonalized Beam Warming pentadiagonal scheme is employed along with dual-time stepping. For the turbulence and transition modeling, OVERFLOW uses either the Amplification Factor Transport (AFT) model (Ref. 18) associated to the Spalart-Allmaras (SA) turbulence model (Ref. 19), or the Langtry-Menter (LM) transition model (Ref. 3) associated to the $k-\omega$ SST turbulence model (Ref. 20). The initial LM model has been modified to guarantee Galilean invariance (Ref. 10) that is required for rotor flow. This modified model is referred to as LM-G thereafter. Furthermore, the extension of the LM model to crossflow transition correlation (Ref. 21) has been considered and will be evaluated. The LM-G model extended to crossflow correlation will be noted LM-G-CF. The turbulence level involved in the correlation calculation is assumed as uniform and set to 0.08% with respect to hover tip speed (ΩR). For both turbulence models (SA and SST), the DDES modeling is used so that the turbulence model is only activated in the attached boundary layers. For the FUN3D unstructured grid flow solver that is used around the ROBIN-Mod7 fuselage, the convective flux is discretized with a second order Roe's scheme with MUSCL (Monotone Upwind Scheme for Conservation Laws) reconstruction, while the viscous flux uses a second-order central scheme. Temporal integration is based on a second-order backward-Euler scheme BDF2opt with dual-time stepping. The flow is assumed as fully turbulent around the fuselage.

The off-body grids are treated as inviscid with the SAM-Cart solver, with a fifth order central scheme for the convective fluxes and a third-order Runge-Kutta explicit scheme for the time integration.

The Helios grid is shown in Figure 3 and the characteristics of the grid are provided in Table 2. Each blade grid is composed of 17.7 million points, the fuselage grid consists of 2.5 million points while the off-body Cartesian grid counts 188 million points.

The time step corresponds to an azimuthal increment of 0.25 deg, with 60 sub-iterations in OVERFLOW and 30 in FUN3D.

3.2. elsA setup

ONERA applied the elsA solver (Ref. 22) which discretizes the Navier-Stokes equations with finite volume approach. A Chimera technique is used, with structured body-fitted grids around the blade and the fuselage and a Cartesian background grid in the wake regions. The convective fluxes are discretized with a second order Jameson scheme using artificial dissipation coefficients $\chi^{(2)} = 0.5$ and $\chi^{(4)} = 0.008$. Second order central scheme is employed for the the viscous fluxes. Time integration is performed with an iterative Gear second order implicit scheme and Newton sub-iterations.

For the transition modeling, both TC and LM models are evaluated. For the LM model, the Galilean invariance correction proposed by Jain (Ref. 10) is used and the model is referred to as LM-G. The crossflow correlation will also be considered (LM-G-CF) and discussed in the validation section thereafter. Both TC and LM-G methods are coupled with k-ω SST turbulence model (Ref. 20). The turbulence level used for the computation of the transition correlations is considered as uniform and equal to 0.08%. Unlike Helios, no DDES approach is involved here. Furthermore, the flow in the off-body grids is assumed as viscous and turbulent, instead of inviscid for Helios.

The effect of the grid resolution is investigated in the next section with elsA code. Three blade grids are built with increasing resolution. These grids are shown in Figure 4 and referred-to as "coarse", "medium" and "fine" grids. The grid characteristics are provided in Table 2. The coarse grid is composed of 6.45 million points, with 269 points around the blade chord, 177 in the span direction and 101 in the wall normal direction. The medium grid is mainly refined in the chordwise direction with 574 points while the resolutions in the span and wall normal directions are almost the same. The fine grid is similar to the medium grid except in the wall normal direction where 131 points is used. For all blade grids, the off-body grid is kept identical and consists of 27 million points with a minimum grid resolution of 8% of chord around the rotor. Initial simulations are performed without fuselage with the three different blade grids. Then, with the finest blade grid, a third simulation including the fuselage is performed. A view of the computational domain with and without the fuselage is shown in Figure 5.

All the elsA simulations are performed with an azimuthal time step of 0.25 deg and 40 Newton sub-iterations.

The blade deformation is not taken into account in the elsA simulations. The rigid blade motion defined in Table 3 is

prescribed in all elsA simulations. In order to assess the relevance of this simplification, the effect of the blade deformation will be investigated thereafter with Helios code.

3.3. Calculation of the transition positions

As discussed in Ref. 12, the extraction of the transition position from a simulation based on the LM model is not straightforward. The quantities provided by the model such as the intermittency, the turbulent kinetic energy or the eddy viscosity ratio are equal to zero at the blade wall whether the boundary layer is laminar or turbulent. Therefore, the transition position cannot be easily deduced from any wall quantities, and it is preferable to use the three-dimensional field in order to calculate the state of the boundary layer. Even based on the three-dimensional field, the way to define the transition position is not straightforward and several strategies can be developed. The ones used by U.S. Army and ONERA have been set up to be similar in order to have a fair comparison, but some slight differences still exist.

At ONERA, the calculation of the transition position is done as follows: At each time step, an extraction of an iso-j surface of the three-dimensional blade grid is done, j being the grid index in the wall normal direction. Several lines are then extracted from this surface at several radial sections from the blade root to the blade tip. Along these lines, the flow solution is scanned from the leading edge toward the trailing and transition position x_{tr}/c is defined as the chordwise position where turbulent kinetic energy normalized by the squared tip hover velocity $k/(R\Omega)^2$ reaches a threshold value set to 1.5%. Since the transition position can depend on the choice of the j-index, this process is repeated for several values of j and the minimum x_{tr}/c is retained as the final transition position. The influence of the $k/(R\Omega)^2$ threshold will be discussed in section 4.4.

At U.S. Army, the strategy used to calculate the transition position is defined as follows: At each time step, several iso-radius surfaces are extracted from the three-dimensional blade grid at several radial position. On this radial plane, and for several chordwise positions starting from the leading toward the trailing edge, the flow solution is scanned in the wall normal direction along the grid line up to a maximum number of j-index. If the turbulent kinetic energy $k/(R\Omega)^2$ gets higher than a critical level along this grid line, the current chordwise position is defined as the transition position x_{tr}/c for this radial position. The process is then repeated for all the radial positions along the blade and for each time step. The critical level of $k/(R\Omega)^2$ is here set to 10^{-5} which is much lower than the value of 1.5% used with elsA. The choice of the critical value of $k/(R\Omega)^2$ has been chosen for both codes to be a relevant indicator of the raise of turbulence inside the boundary layer, where the eddy viscosity ratio increases from being $(\mu_t/\mu)_\infty \ll 1$ in the laminar region to growing to $O(1)$ at the transition point. This value is however different between the codes, probably because the freestream turbulent kinetic energy k_∞ has been set to different values. In Helios, $k_\infty/(R\Omega)^2 = 1 \times 10^{-6}$ while in elsA $k_\infty/(R\Omega)^2 = 1.5 \times 10^{-8}$. Furthermore, the freestream value of turbulent dissipation rate ω_∞ is also different between the code. In Helios, it is deduced from a freestream eddy viscosity ratio of $(\mu_t/\mu)_\infty = 1$ while elsA uses $(\mu_t/\mu)_\infty = 0.1$.

4. VALIDATION

In previous studies (Ref. 12), LM model has shown to be very sensitive to the numerical parameters, especially the grid resolution. Therefore, in this section, we propose, in a first step, to investigate the effects of several elements of the numerical setup such as the grid resolution, the fuselage modeling and the blade deformation on the solution provided by LM model. Furthermore, the critical value of turbulent kinetic energy $k/(R\Omega)^2$ used to define the transition position has been set arbitrarily. The sensitivity of the results with respect to this value will also be analyzed in the last part of this section.

4.1. Grid sensitivity analysis

The grid sensitivity of LM model is performed with elsA CFD code. The transition model is expected to be mainly affected by the grid resolution inside the boundary layers while the grid resolution in the wake is expected to have only a small effect. Therefore, only the resolution of the blade body-fitted grids is analyzed and the background grid is kept identical. As previously introduced, the three grid levels are presented in Table 2 and shown in Figure 4. The blade is considered as rigid and the same flap, lag and pitch angles as provided in Table 3 are imposed for all the simulations. Each of the simulations were initially run as a fully turbulent for 3 or 4 rotor revolutions using an azimuthal time step of 1 deg. Then the simulations were continued for another 3 or 4 revolutions with the LM-G model using a reduced time step of 0.25 deg.

The transition maps obtained with the three grid levels are compared to the experimental data in Figure 6. The experimental data (Figure 6.a) shows a rearward motion of the transition position on the advancing blade side up to $\psi = 120°$ where it reaches its maximum position located between 70% and 90% of chord at the blade tip. Around 180° of azimuthal, the transition rapidly moves back toward the

leading-edge region to locate around 10% of chord along a large part of the retreating blade side. For all grids, the simulations provide this global trend. However, the coarse grid (Figure 6.b) shows some oscillations of the transition position x_{tr}/c in the first quadrant for $0° \leq \psi \leq 60°$ that seem to be due to a numerical artifact. Refining the grid in the chordwise direction (Figure 6.c) eliminates these oscillations, but an unexpected result remains for $30° \leq \psi \leq 60°$ where the transition moves rearward in the thin region close to the blade tip. Refining the grid in the wall normal direction (Figure 6.d) reduces the extent of this region, although the problem remains. The fine grid also results in the transition location moving rearwards for $90° \leq \psi \leq 180°$, which improves the prediction at the blade tip ($r/R \geq 0.9$) but deteriorates the prediction at the most inboard sections ($r/R \leq 0.9$). The azimuthal evolution of the transition position for the section $r/R = 0.85$ shown in Figure 7 confirms these observations. Refining the grid clearly reduces the spurious oscillations of x_{tr}/c for $0° \leq \psi \leq 60°$, but one single peak remains at $\psi = 60°$ even for the finest grid. The rapid motions of transition that occur at 90° and 180° of azimuth are well captured by all the simulations. For $90° \leq \psi \leq 180°$, while the coarse and medium grids provide a good prediction of x_{tr}/c, the fine grid gives a "swerve" of the transition towards the trailing edge that is not expected. On the retreating blade side, the prediction is less sensitive to the grid resolution and all the simulations provide a good agreement with the experiment. For the rest of the analysis, all the elsA simulations will be performed with the fine blade grid.

4.2. Influence of the fuselage

The previous simulations were only considering an isolated rotor while the experiment was carried out with the ROBIN-Mod 7 fuselage below the rotor. The presence of the fuselage could modify the downwash of the rotor that could change the evolution the transition on the rotor blade. To evaluate this potential effect, a new simulation is performed with a fuselage body-fitted grid shown in Figure 5.b composed of 0.9 million points. For this simulation, the blades are meshed with the finest refinement level and the background grid is kept almost identical. The pitch, flap and lead-lag angles are prescribed to the same values as used previously. The numerical results obtained with the fuselage are compared to the isolated rotor case and to the experimental data in the form of transition maps in Figure 8. As can be seen, the effect of the fuselage is minor. A more accurate comparison is shown in Figure 9 for the section located at $r/R = 0.85$. This confirms that the very slight change of transition position between 90° and 180° of azimuth is not significant enough to consider the fuselage as an important element of the transition process of the blade boundary layers.

4.3. Blade deformation effect

The simulations performed previously require lots of computing resources since the grid resolution is very fine and the number of the sub-iterations at each time step is very high. In order to reduce the computational effort, all the elsA simulations have been performed assuming a rigid blade, while all the Helios simulations have taken into account the blade elasticity. However, the blade deformation, especially in torsion, could change the angle of attack along the blade sections and affect the transition position. In order to quantity the influence of blade deformation on the transition position, Helios LM-G simulations have been performed with both rigid and elastic blade models, and the transition positions thus obtained are compared in Figure 10 for a section located at $r/R = 0.85$. The results show that the effect of blade deformation is not negligible. The rigid blade model gives a transition motion with a phase lead compared to the elastic blade results. Furthermore, the most rearward transition position is moved slightly frontward with rigid blade. At last, the rigid blade model make two oscillations appear during the rearward transition motion on the advancing blade side. This phenomenon looks similar to the oscillations also observed with elsA in Figure 7 and Figure 9 between 90° and 110° of azimuth. However, the rigid blade simulation with Helios does not reproduce the peak observed with elsA at $\psi = 60°$. Furthermore, some significant discrepancies still remain between the Helios rigid simulation and elsA simulations. Therefore, we can consider that the blade deformation does influence the transition position but cannot be considered as the main reason of the discrepancies between Helios and elsA. Another possible reason is related to the way the transition position is computed. This point is developed in the next section.

4.4. Sensitivity with respect to the transition position calculation

As presented in section 3.3, the way to define the transition position is based on a critical value of turbulent kinetic energy k. Since this value is to be set arbitrary, it is required to evaluate the sensitivity of the transition position with respect to this value. This investigation has been performed with elsA code with four values of $k/(R\Omega)^2$: 0.15%, 0.35%, 0.75 and 1.5%. An *a posteriori* analysis showed that the extreme values, 0.15% and 1.5%, correspond to an eddy viscosity ratio μ_t/μ of 0.1 and 1 respectively. The transition positions calculated at $r/R = 0.85$ with the four

threshold values of $k/(R\Omega)^2$ are depicted in Figure 11. The results show that the critical level of turbulent kinetic energy significantly affects the transition position, especially in the region where the numerical prediction shows some spurious results. Decreasing the $k/(R\Omega)^2$ threshold reduces the peak observed around 60° of azimuth, which improves the prediction. However, it also leads to an earlier transition around $\psi = 80°$ and a delay of the rearward transition motion for $90° \leq \psi \leq 110°$, which slightly deteriorates the prediction. The large peak observed between 120° and 130° of azimuth is also significantly reduced with the low threshold of $k/(R\Omega)^2$, which gives a better agreement with experiment. This analysis shows that the way to post-process the results in order to calculate the transition with LM model can be as significant as the effect of the blade deformation and the grid resolution. Therefore, the results presented thereafter have to be considered with a certain margin of uncertainty and the validations are to be interpreted carefully. For the rest of the analysis, we have decided to use $k/(R\Omega)^2 = 1.5\%$ for the elsA simulations although it does not provide the best agreement with experiment. This value has been retained because it corresponds to a significant increase of eddy viscosity ratio (μ_t/μ) to $O(1)$. At lower threshold levels, the results show that transition can be detected for $\mu_t/\mu \ll 1$, which cannot be reasonably considered as turbulent according to the authors' opinion.

Note that the final threshold value selected in elsA is consistent with the Helios simulations in terms of the threshold eddy viscosity at transition. In Helios the freestream value of $k/(R\Omega)^2$ was set to 1×10^{-6} and the freestream eddy viscosity ratio of $(\mu_t/\mu)_\infty$ was set to 1.0. The transition threshold for transition for $k/(R\Omega)^2$ was set to be an order of magnitude higher, $= 1 \times 10^{-5}$, which amounted to an eddy viscosity ratio growing from $\ll 1$ in the laminar region to $O(1)$ at the transition point.

5. ANALYSIS OF THE TRANSITION MODELS

In this section we evaluate different transition models using Helios and elsA. For the Helios simulations, a fine grid resolution for the blade with elastic deformations and a fuselage model will be used, as required by the sensitivity analysis presented previously. For elsA simulations, a fine grid resolution for the blade, and a fuselage model will be considered, but the blade deformation will be neglected because of technical constraints related to importing prescribed blade deformations in elsA. For Helios, the (Amplification Factor Transport) transition model based on SA turbulence model will be evaluated. For elsA, the semi-empirical Transition Criteria (TC) approach will be used. For both Helios and elsA codes, the Langtry-Menter model including the Galilean invariance correction will be used in its standard version (LM-G) and including crossflow correlation (LM-G-CF). All LM model are coupled to the SST turbulence models.

The Helios results are presented in Figure 12 in the form of transition maps. The overall trends are captured very well by all the transition models. AFT seems to predict a thin region where the transition is slightly too delayed for $90° \leq \psi \leq 120°$ (Figure 12.b). LM-G model does not show this behavior in this azimuthal region and shows a better agreement with the experiment (Figure 12.c). However, a thin strip of delayed transition remains at 95% of radius in the first quadrant that is not observed in the experiments. Including the crossflow transition correlation corrects this problem, which improves the prediction (Figure 12.d). However, LM-G-CF also tends to predict an earlier transition for $90° \leq \psi \leq 180°$, which deteriorates the prediction compared to the initial model LM-G. A comparison of the transition predictions along the section located at 85% of radius is presented in more detail in Figure 13. All the models provide similar results that are in very good agreement with experiments. The main difference between the models concerns the position of the transition reached on the advancing blade side between 90 and 180° of azimuth. AFT presents a first peak at $\psi = 120°$ that does not correspond to the experimental observations. After this peak, AFT predict a transition located between 60% and 70% of chord, which is similar to LM-G and LM-CF models and in good agreement with the experiments. On the retreating blade side, all the models predict the evolution of the transition moving towards the leading edge, and the agreement with the experimental data is good.

The transition maps obtained with elsA simulations are presented in Figure 14. The TC approach significantly underestimates the extent of the region where the transition moves rearwards for $90° \leq \psi \leq 180°$ (Figure 14.b), while the trend is correct in the rest of the rotor disk. LM-G model predictions show a better agreement with experiment and a global trend that is similar to the one provided by Helios (Figure 12.c). However, the LM-G model with elsA provides some differences in the blade tip region between 30 and 60° of azimuth that are not observed in the experiments (Figure 12.a) and not predicted with Helios. Furthermore, the extent of the rearward transition position region for $90° \leq \psi \leq 180°$ seems to be slightly overestimated by elsA compared to the Helios prediction with the same LM-G model. Including the crossflow transition correlation reduced this extent (Figure 12.d), similar to the Helios observations. The predictions of the azimuthal evolution of the

transition at $r/R = 0.85$ are provided in Figure 15. Both LM-G and LM-G-CF show a spurious peak of x_{tr}/c around 60° of azimuth. This behavior differs from the results provided by Helios using the same models. The investigation of the blade deformation effect with Helios code presented in section 4.3 seems to show that the blade rigid model is not responsible for the peak of x_{tr}/c obtained with elsA at $\psi = 60°$. However it could be the reason for the oscillations of the transition position during rearward motion between 90 and 110° of azimuth, as a similar oscillation appears in the Helios rigid blade simulation in Figure 10, although it occurs in phase lead. Despite these discrepancies, the rearward and frontward transition motions (observed respectively at $\psi = 90°$ and $\psi = 180°$) are correctly captured by the LM-G model with the elsA simulation. The crossflow correlation slightly decreases the transition position between 90° and 180°, but it is not obvious to conclude that the prediction is improved. As previously observed, TC approach significantly underestimated the transition in this azimuthal region, while it gives a good prediction on the rest of the azimuths, similar to the LM-G and LM-G-CF models.

In order to complete this analysis, a view of the laminar and turbulent regions on the blade upper side is proposed at $\psi = 45°$ and $\psi = 135°$ in Figure 16 and Figure 17, respectively, for the Helios simulations, and in Figure 18 and Figure 19, respectively, for the elsA simulations. At $\psi = 45°$, both AFT (Figure 16.b) and LM-G (Figure 16.c) with Helios shows a thin strip of laminar flow downstream of the edge of the swept blade tip. This effect is also visible in the experiment (Figure 16.a) but with a smaller extent of the laminar region. LM-G-CF completely removes this laminar zone. ElsA simulation with LM-G shows an exaggeratedly large laminar region in this area (Figure 18.b). LM-G-CF reduces this laminar region (Figure 18.c) but it remains visible with elsA while it disappears with Helios. TC approach gives an almost constant transition position all along the blade span (Figure 18.d). At $\psi = 135°$, the transition has moved rearward to reach 60% to 70% of chord. The overall trends is captured well in all the Helios simulations (Figure 17). With elsA, LM-G and LM-G-CF gives results that are very similar to Helios, while TC approach seems to show intermittent regions of laminar and turbulent flows.

The surface streamlines obtained with LM-G model at the same azimuthal positions ($\psi = 45°$ and $\psi = 135°$) are provided in Figure 20 and Figure 21 respectively. At 45° of azimuth, both Helios and elsA show that the transition is induced by a small laminar separation bubble close to the leading edge (Figure 20). At 135° of azimuth, although Helios and elsA give the same transition position, Figure 21 reveals that Helios predicts an attached flow transition process while elsA shows again a laminar separation bubble. No clear reason for this discrepancy between the codes has been found during this investigation.

A visualization of the flow field obtained with Helios and elsA for the same SST-LM-G model is shown in Figure 22. Since Helios involves an inviscid model and a very fine resolution in the Cartesian grid, more vortical structures appear in the flow, but those are mostly located in the fuselage wake region, while the vortices in the rotor region look similar between the codes. Therefore, we can consider that the induced velocity field in the rotor disk should be similar between Helios and elsA. However, some differences can arise from the fact that the RANS modeling of elsA allows the convection of high turbulence kinetic energy in the rotor wake that can affect the transition process. Since Helios considered the fluid as inviscid in the Cartesian grid, the turbulence is effectively reduced to zero in the wake. This difference could also partially explain some of the discrepancies observed between the codes.

6. CONCLUSIONS

In the frame of a joint research activity between U.S. Army and ONERA, several turbulence transition models have been assessed with two CFD codes, Helios and elsA, for a helicopter rotor in forward flight. Amplification Factor Transport (AFT) model has been evaluated with Helios and Transition Criteria (TC) approach with elsA. Both codes have also investigated Langtry-Menter model with its original transition correlation on one hand (LM-G) and including crossflow transition correlation on the other hand (LM-G-CF). The main conclusions of this large investigation are as follows:

1. Fine grid resolution in the boundary layer is required with LM-G model, while too coarse grids can lead to oscillations of the transition position in the first quadrant of the rotor disk.
2. The downwash flow modification induced by the fuselage does not affect significantly the transition position on the rotor blade.
3. Blade deformation has a noticeable effect on the transition position, although the global trend is identical between rigid and elastic blade models.
4. The strategy used to compute the transition position from LM-G simulations is not straightforward and the transition position can be significantly modified with small changes to the post-processing.

5. Helios simulations show similar transition positions with AFT, LM-G and LM-G-CF that are in good agreement with experiments.
6. elsA simulations show that the TC approach does not accurately predict the rearward motion of the transition on the advancing blade side.
7. elsA simulations provide better agreement with the experiment with the LM-G and LM-G-CF models, compared to the TC approach.
8. The results of Helios and elsA for LM-G and LM-G-CF models are similar but some discrepancies remain. The blade deformation that is not taken into account with elsA can partially explain these discrepancies.

Author contact:

François Richez, francois.richez@onera.fr

ACKNOWLEDGMENTS

The authors would like to acknowledge the U.S./France Project Agreement on Rotary-Wing Aeromechanics and Human Factors Integration Research, a longstanding cooperation between the U.S. Army, ONERA and DGA. A part of the material (Helios calculations) presented in this paper is a product of the CREATE (Computational Research and Engineering for Acquisition Tools and Environments) element of the U.S. Department of Defense HPC Modernization Program (HPCMP). Computational resources for Helios calculations were provided under the HPCMP Frontier program and are gratefully acknowledged.

REFERENCES

1. Arnal D., Habiballah M., and Coustols E., "Laminar instability theory and transition criteria in two and three-dimensional flow," *La Recherche Aérospatiale (English Edition)*, 2:45–63, 1984,
2. Cliquet, J., Houdeville, R. and Arnal, D., "Application of Laminar-Turbulent Transition Criteria in Navier-Stokes Computations," *AIAA Journal*, vol. 46, pp. 1182–1190, May 2008, https://doi.org/10.2514/1.30215
3. Langtry, R.B., and Menter, F.R., "Correlation-Based Transition Modeling for Unstructured Parallelized Computational Fluid Dynamics Codes," *AIAA Journal*, Vol. 47, No. 12, 2009, pp. 2894-2906, https://doi.org/10.2514/1.42362
4. Richez, F., Nazarians, A. and Lienard, C., "Assessment of laminar-turbulent transition modeling methods for the prediction of helicopter rotor performance", Proceedings of the 43rd European Rotorcraft Forum, Milan, Italy, September 12-15, 2017.
5. Weiss, A., Gardner, A. D., Schwermer, T., Klein, C., and Raffel, M., "On the Effect of Rotational Forces on Rotor Blade Boundary-Layer Transition", *AIAA Journal*, Vol. 57, (1), 2019. https://arc.aiaa.org/doi/10.2514/1.J057036
6. Kaufmann, K., Stroër, P., Richez, F., Lienard, C., Gardarein, P., Krimmelbein, N. and Gardner, A., D., "Validation of boundary-layer-transition computations for a rotor with axial inflow", Proceedings of the Vertical Flight Society 75th Annual Forum & Technology Display, Philadelphia, Pennsylvania, May 13–16, 2019.
7. Jain, R., "CFD Hover Performance and Transition Predictions on the PSP and HVAB Rotors using CREATE™-AV Helios", Proceedings of the AIAA SciTech Forum, San Diego, CA, January 3-7, 2022, https://doi.org/10.2514/6.2022-1549
8. Overmeyer, A. D., and Martin, P. B., "Measured Boundary Layer Transition and Rotor Hover Performance at Model Scale" Proceedings of the 55th AIAA SciTech Forum, Grapevine, TX, January 9–13, 2017. https://doi.org/10.2514/6.2017-1872
9. Weiss, A., Wolf, C.C., Kaufmann, K., Braukmann, J.N., James T. Heineck, J.T., and Raffel, M., "Unsteady boundary-layer transition measurements and computations on a rotating blade under cyclic pitch conditions," *Experiments in Fluids*, Vol. 61, 2020, https://doi.org/10.1007/s00348-020-2899-7
10. Jain, R., "Computational Fluid Dynamics Transition Models Validation for Rotors in Unsteady Flow Conditions," *Journal of Aircraft*, Vol. 59, No. 4, July-August 2022, https://doi.org/10.2514/1.C036580
11. Carnes, J., and Coder, J. G., "Numerical Investigation of Unsteady Boundary Layer Transition on a Dynamically Pitching Rotor," *Journal of the American Helicopter Society*, Vol. 67, Aug. 2021, Paper 012003, https://doi.org/10.4050/JAHS.67.012003
12. Richez, F. and Jain, R., "Prediction of the laminar-to-turbulent transition position on a helicopter rotor blade with cyclic pitch variation", Proceedings of the Vertical Flight Society's 79th Annual Forum & Technology Display, West Palm Beach, FL, USA, May 16-18, 2023.
13. Gardner, A. D., Weiss, A., Heineck, J. T., Overmeyer, A. D., Spooner, H. R., Jain, R. K., Wolf, C. C. and Raffel, M., "Boundary Layer Transition Measured by DIT on the PSP Rotor in Forward Flight", *Journal of the American Helicopter Society*, Vol. 66, No. 2, April 2021, https://doi.org/10.4050/JAHS.66.022008.
14. Wissink, A. M., Sitaraman, J., Jayaraman B., Beatrice, R., Lakshminarayan, V. K., Potsdam M., Jain R., Bauer, A., and Strawn, R., "Recent Advancements in the Helios Rotorcraft Simulation Code," AIAA 2016-0563, 54th AIAA Aerospace Sciences Meeting, AIAA SciTech Forum, San Diego, California, January 4-8 2016.
15. Nichols, R.H., and Buning, P. G., "OVERFOW User's Manual, Version 2.2," NASA Langley Research Center, Hampton, VA, August 2010.

16. Biedron, R.T., Carlson, J., Derlaga, J.M., Gnoffo, P.A., Hammond, D.P., Jacobson, K.E., Jones, W.T., Kleb B., Lee-Rausch, E.M., Nielsen E.J., Park, M.A., Rumsey, C.L., Thomas, J.L., Thompson, K.B., Walden A.C., Wang L., and Wood, W.A., FUN3D Manual: 13.7, *NASA TM-20205010139*, November 2020, https://fun3d.larc.nasa.gov.
17. Saberi, H. A., Hasbun, M., Hong, J., Yeo, H., and Ormiston, R.A., "RCAS Overview of Capabilities, Validations, and Applications to Rotorcraft Problems," American Helicopter Society 71st Annual Forum Proceedings, Virginia Beach, Virginia, May 5-7, 2015, Virtual, Paper No. 71-2015-0328.
18. Coder, J.G., "Further Development of the Amplification Factor Transport Transition Model for Aerodynamic Flows," SciTech 2019 Forum, San Diego, California, January 7-11 2019, AIAA Paper 2019-0039, https://doi.org/10.2514/6.2019-0039.
19. Allmaras, S.R., Johnson, F.T., and Spalart, P.R., "Modifications and Clarifications for the Implementation of the Spalart-Allmaras Turbulence Model," 7th International Conference on Computational Fluid Dynamics, ICCFD7-1902, Big Island, Hawaii, July 2012
20. Menter, F.R., Kuntz, M., and Langtry, R., "Ten Years of Industrial Experience with the SST Turbulence Model," *Turbulence, Heat and Mass Transfer 4*, ed: Hanjalic K., Nagano Y., and Tummers M., Begell House, Inc., 2003, pp. 625-632.
21. Langtry, R.B., Sengupta, K., Yeh, D.T., and Dorgan, A.J., "Extending the γ-$Re_{\theta t}$ Local Correlation based Transition Model for Crossflow Effects," 45th AIAA Fluid Dynamics Conference, AIAA Paper 2015-2474, Dallas, Texas, June 2015 https://doi.org/10.2514/6.2015-2474
22. Cambier, L., Heib, S., Plot, S., "The ONERA *elsA* CFD software: input from research and feedback from industry," *Mechanics & Industry*, Vol. 14 (3), 2013, pp. 159-174.

Table 1: PSP rotor blade characteristics.

Radius, R	1.7018 m (67 in)
Reference chord	0.13843 m (5.45 in)
Tip chord	0.08306 m (3.27 in)
Tip sweep (quarter chord)	30° at 0.9504 R
Tip taper ratio	0.60
Twist	−14°, linear
Airfoils	RC series
Number of blades	3
σ	0.0757
Lag/flap/pitch hinge locations	0.0889 m (3.5 in)

Table 2: Grid characteristics.

		Helios	elsA Coarse Grid	elsA Medium Grid	elsA Fine Grid
Blade grid	Total number of points per blade	17.7M	6.45M	16.7M	21.65
	Number of points around the chord	517	269	574	574
	Number of points in the wall normal	104	101	101	131
	Number of points in the span direction	251	177	197	197
Background grid	Total number of points	188M	27M	27M	27M
	Finest grid resolution	5%c	8%c	8%c	8%c
Fuselage grid	Total number of points	2.5M	-	-	0.9M

Table 3: pitch, flap and lead-lag angles prescribed for the rigid blade simulations.

Pitch	$\theta_0 = 9.71°$	$\theta_{1c} = 3.58°$	$\theta_{1s} = -7.37°$
Flap	$\beta_0 = 4.33°$	$\beta_{1c} = 0°$	$\beta_{1s} = 0°$
Lead-lag	$\delta_0 = -4.18°$	$\delta_{1c} = 0.396°$	$\delta_{1s} = -0.252°$

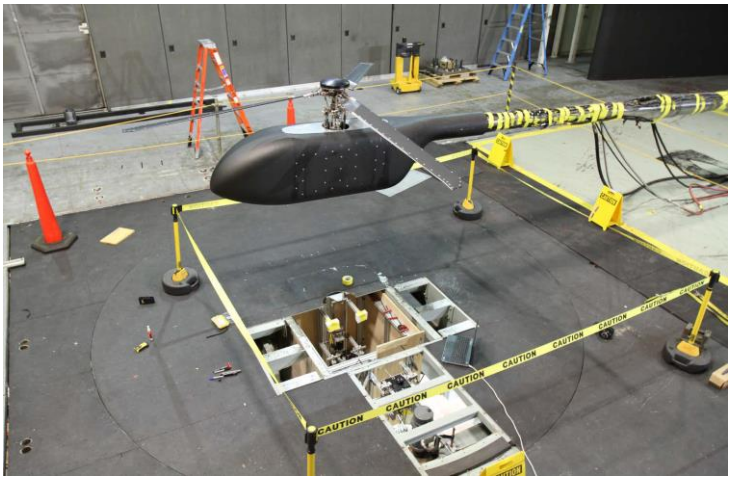

Figure 1: Experimental setup of the PSP three-blade rotor mounted on the Robin-Mod 7 fuselage in the NASA Langley 14- by 22-Foot Subsonic Tunnel.

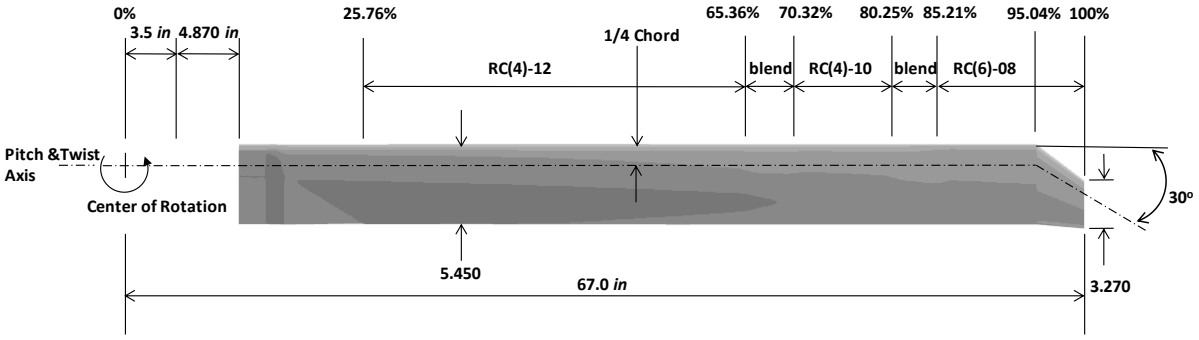

Figure 2: Description of the PSP rotor blade.

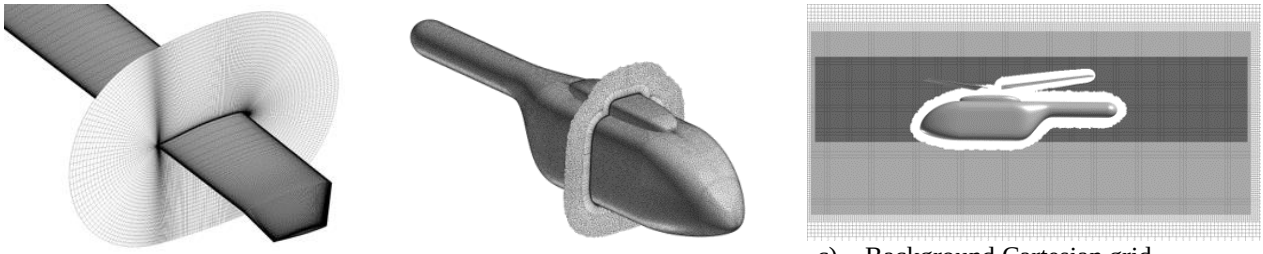

a) Blade structured grid b) Fuselage unstructured grid c) Background Cartesian grid

Figure 3: Blade, fuselage and Background grids (Helios).

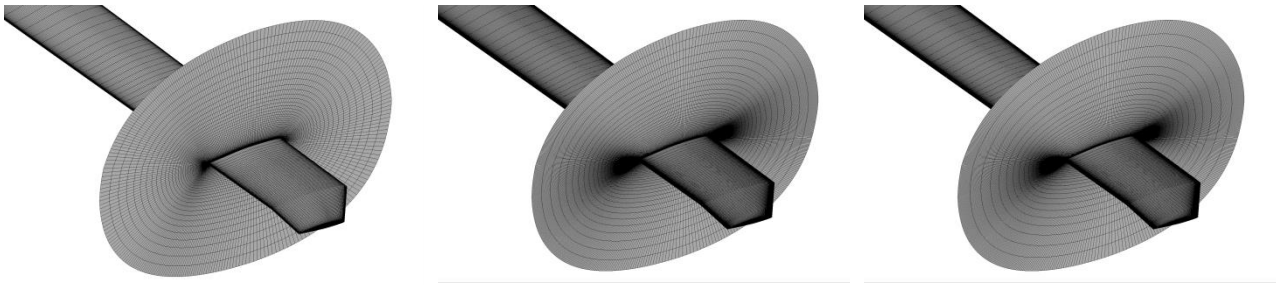

a) Coarse blade grid b) Medium blade grid c) Fine blade grid

Figure 4: Resolution of the blade grids (elsA).

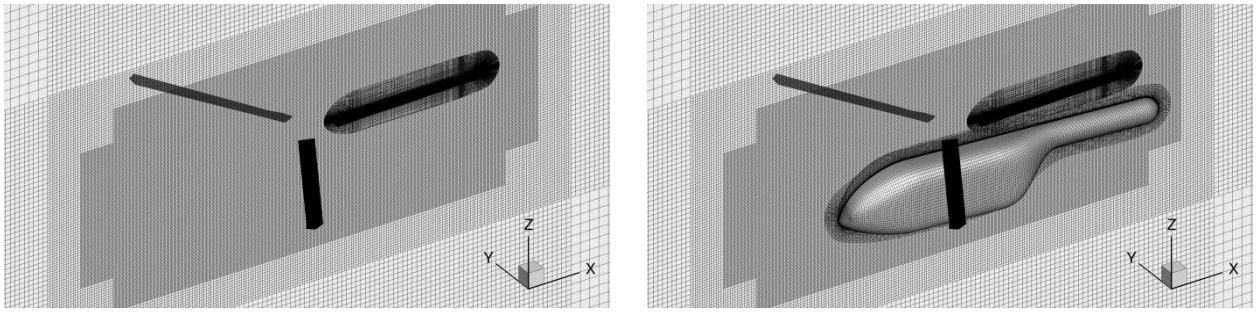

a) Isolated rotor (fine blade grid) b) Rotor with fuselage (fine blade grid)

Figure 5: Body-fitted and background grids with and without fuselage (elsA).

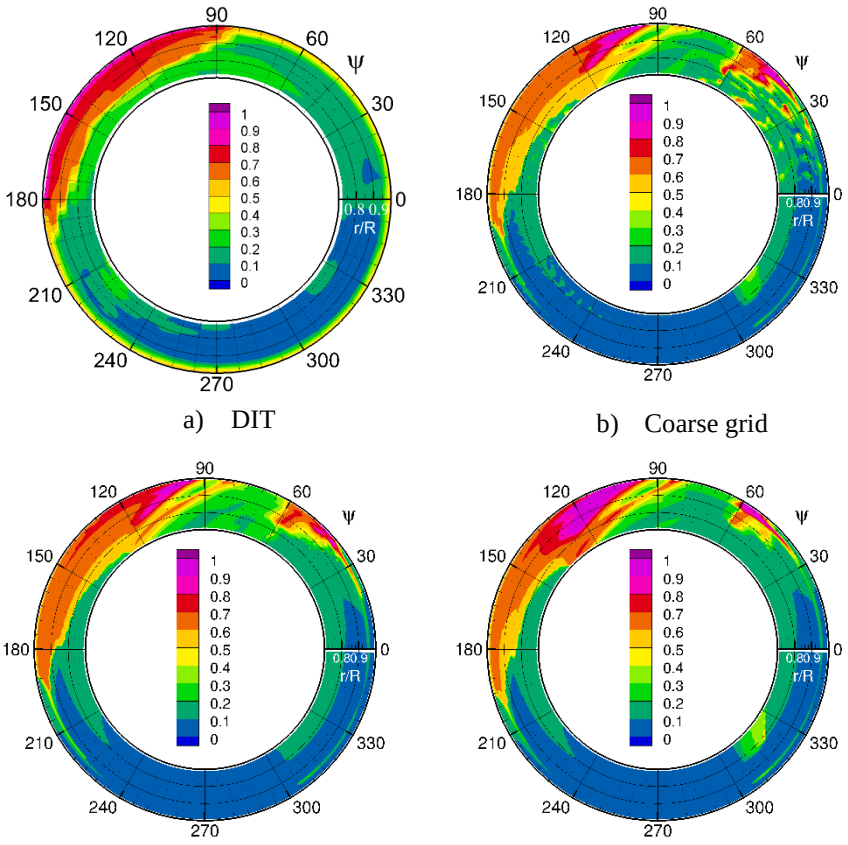

a) DIT b) Coarse grid

c) Medium grid d) Fine grid

Figure 6: Grid resolution effect on the transition rotor map of x_{tr}/c (elsA SST-LM-G).

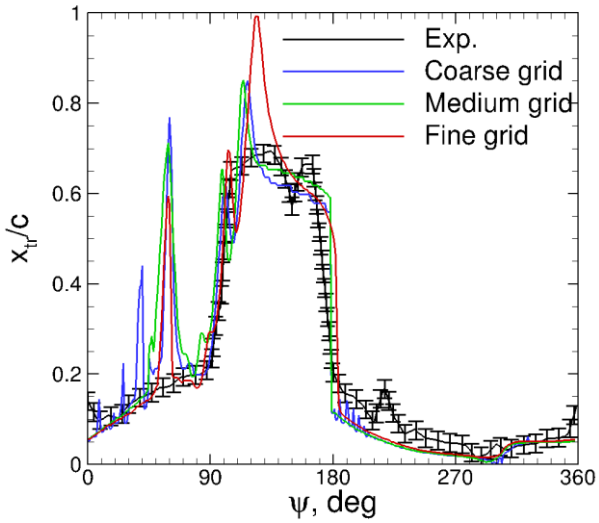

Figure 7: Grid resolution effect on the transition position at $r/R = 0.85$ (elsA SST-LM-G).

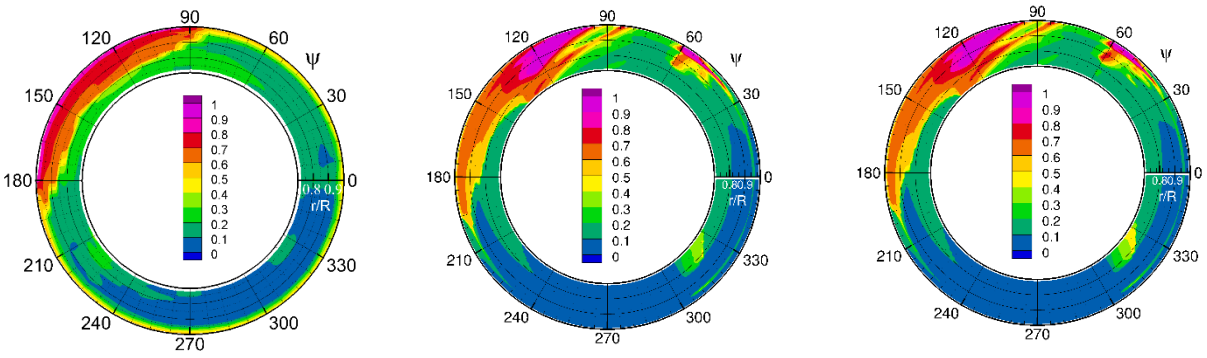

a) DIT b) Isolated rotor c) Rotor with fuselage

Figure 8: Fuselage effect on the transition rotor map of x_{tr}/c (elsA SST-LM-G).

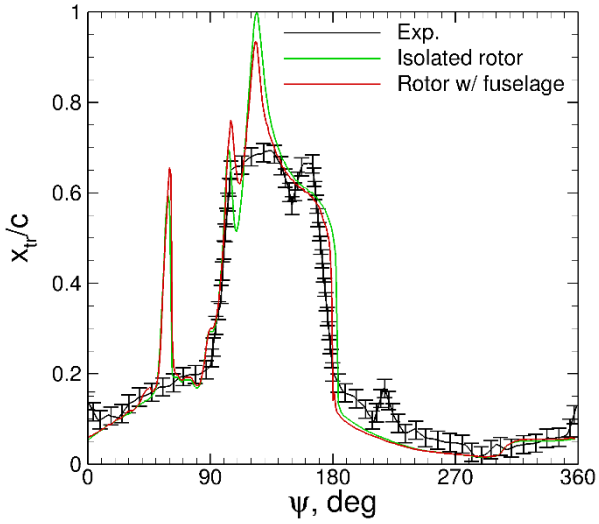

Figure 9: Fuselage effect on the transition position at $r/R = 0.85$ (elsA SST-LM-G).

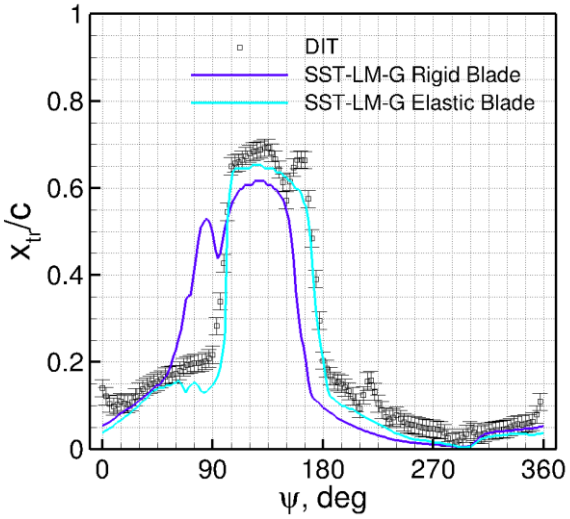

Figure 10: Blade deformation effect on the transition position at $r/R = 0.85$ (Helios SST-LM-G).

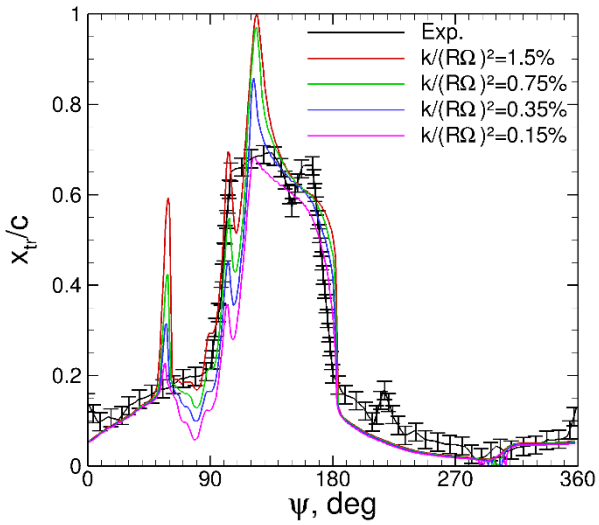

Figure 11: Effect of the critical turbulent kinetic energy $k/(R\Omega)^2$ used to define the transition position at the section $r/R = 0.85$ (elsA SST-LM-G).

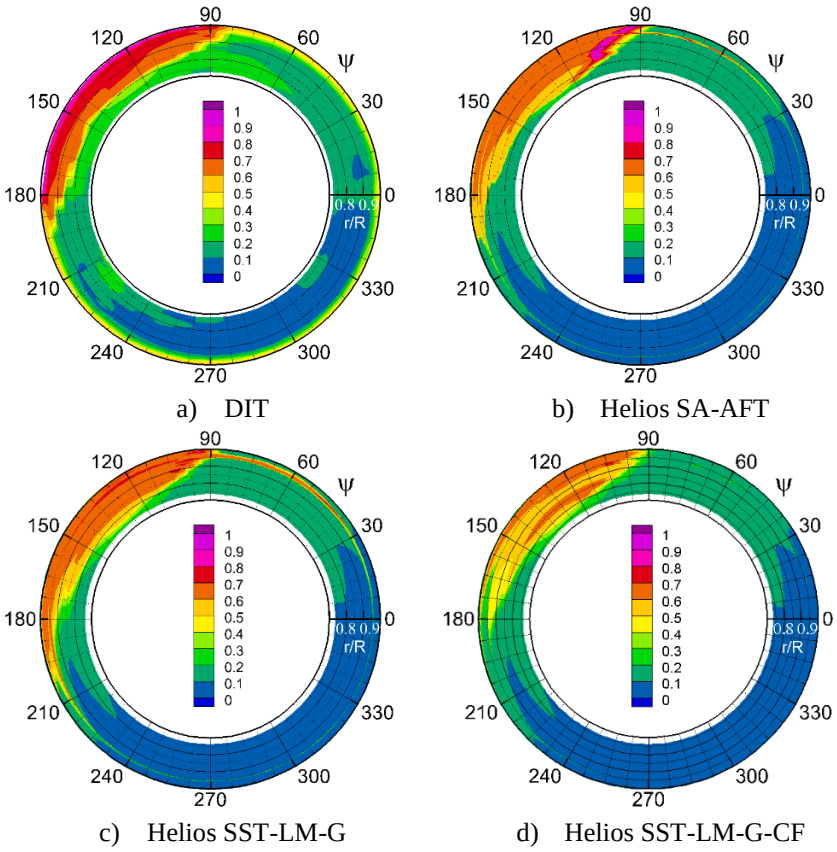

Figure 12: Transition maps of x_{tr}/c with different transition models (Helios).

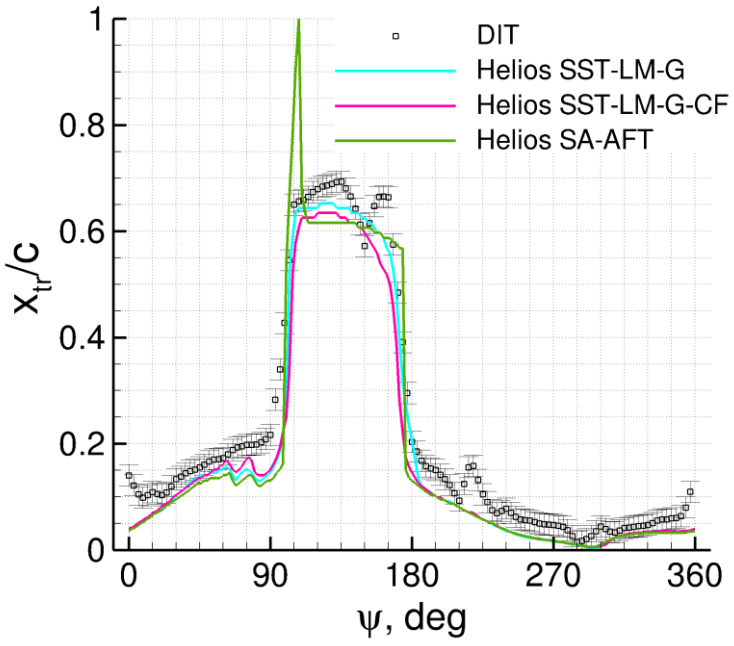

Figure 13: Prediction of the transition position at $\mathrm{r/R} = 0.85$ for different transition models with Helios.

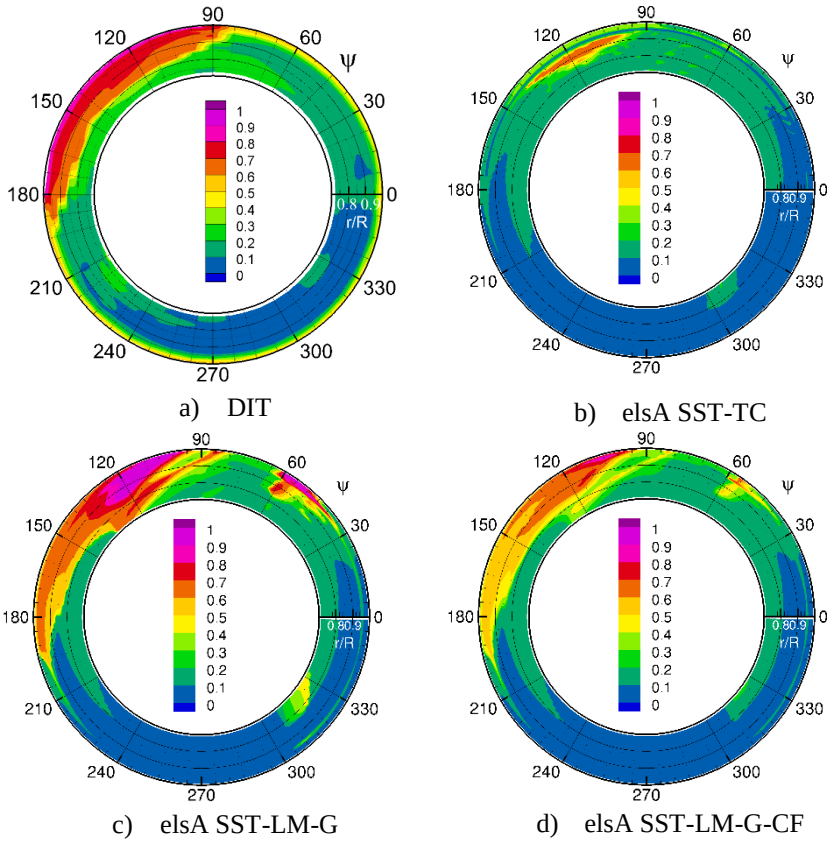

Figure 14: Transition maps with different transition models (elsA).

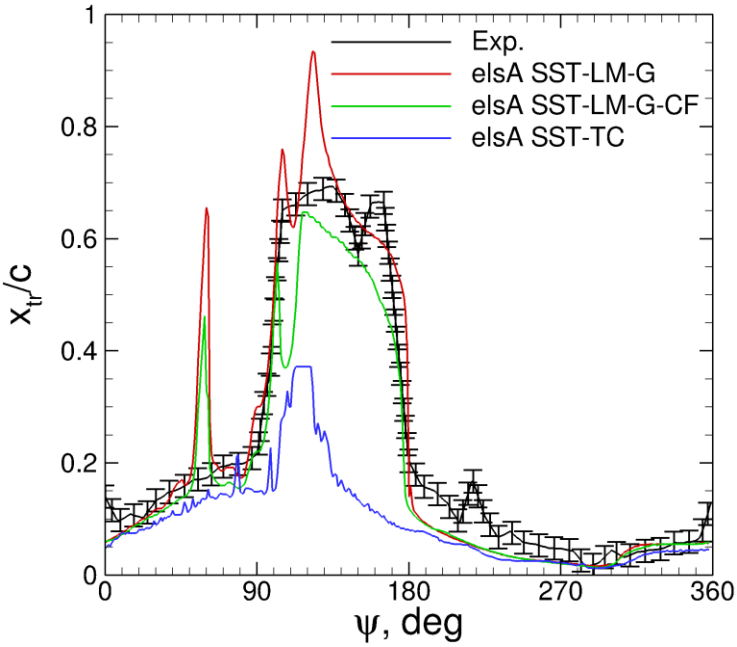

Figure 15: Prediction of the transition position at r/R=0.85 for different transition models with elsA.

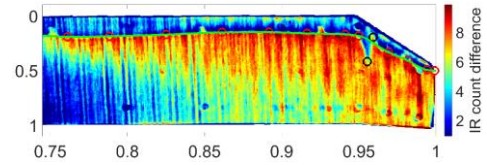

a) DIT measurements

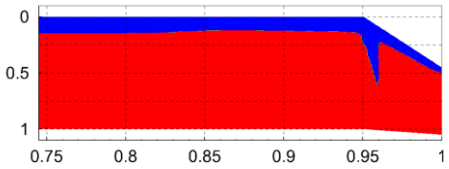

b) Helios SA-AFT

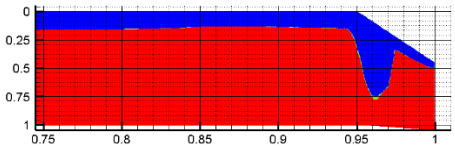

c) Helios SST-LM-G

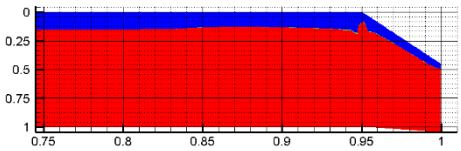

d) Helios SST-LM-G-CF

Figure 16: Laminar (blue) and turbulent (red) regions of the boundary layer at $\psi = 45°$

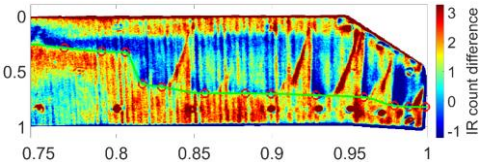

a) DIT measurements

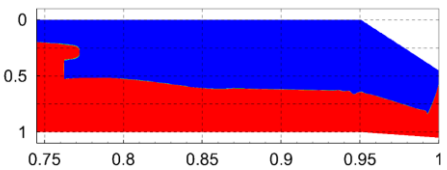

b) Helios SA-AFT

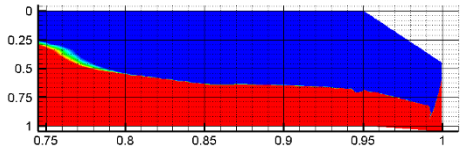

c) Helios SST-LM-G

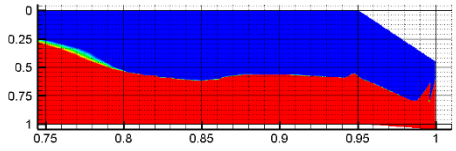

d) Helios SST-LM-G-CF

Figure 17: Laminar (blue) and turbulent (red) regions of the boundary layer at $\psi = 135°$

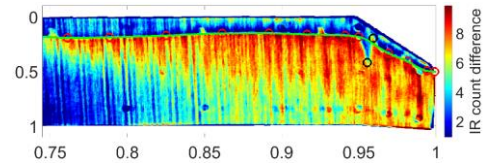

e) DIT measurements

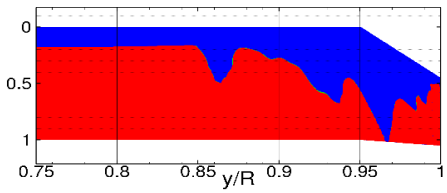

f) elsA SST-LM-G

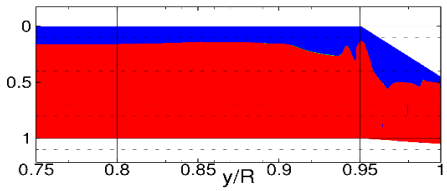

g) elsA SST-LM-G-CF

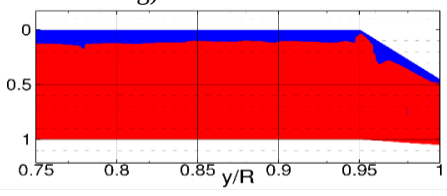

h) elsA SST-TC

Figure 18: Laminar (blue) and turbulent (red) regions of the boundary layer at $\psi = 45°$

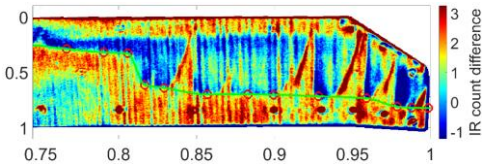

e) DIT measurements

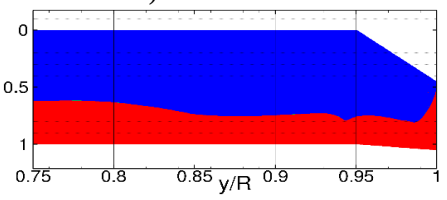

f) elsA SST-LM-G

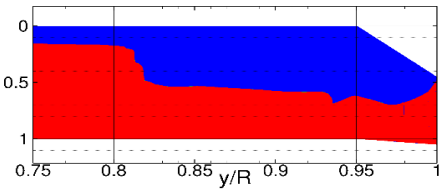

g) elsA SST-LM-G-CF

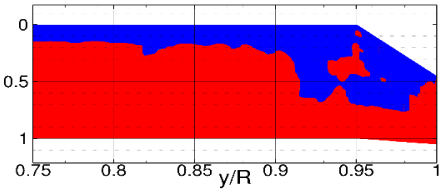

h) elsA SST-TC

Figure 19: Laminar (blue) and turbulent (red) regions of the boundary layer at $\psi = 135°$

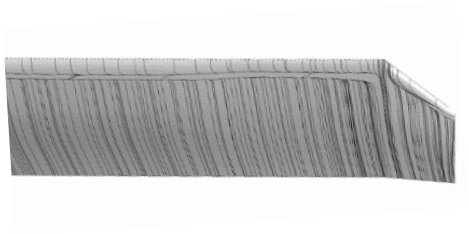

a) Helios SST-LM-G

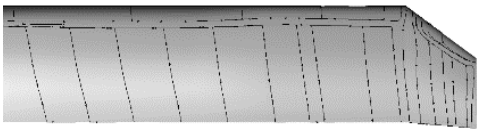

b) elsA SST-LM-G

Figure 20: Skin friction lines at $\psi = 45°$

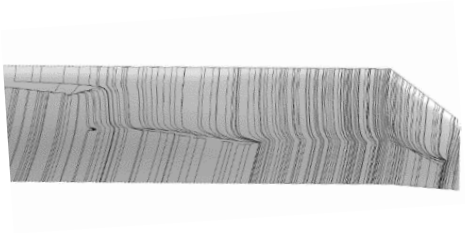

a) Helios SST-LM-G

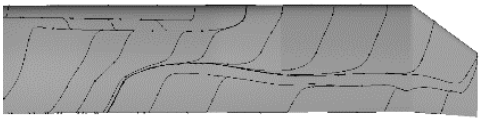

b) elsA SST-LM-G

Figure 21: Skin friction lines at $\psi = 135°$

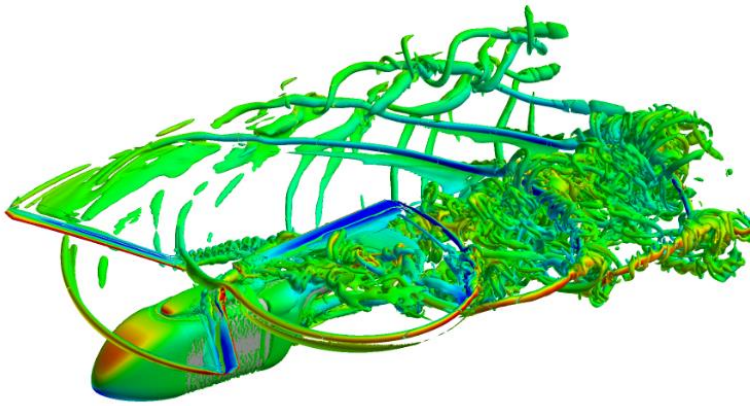

a) Helios ($Q/\Omega^2 = 1$)

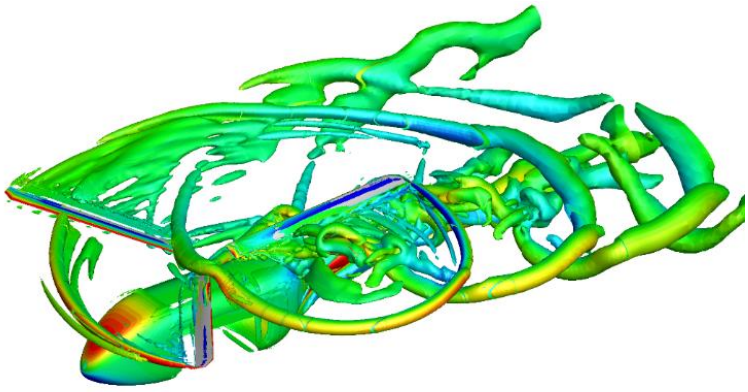

b) elsA ($Q/\Omega^2 = 0.15$)

Figure 22: Iso-contour of Q-criterion colored by the downwash (SST-LM-G).